

Article

# Investigation on the Microstructure and Wear Behavior of Laser-Cladded High Aluminum and Chromium Fe-B-C Coating

Jingjing Li <sup>1,2</sup>, Jiang Ju <sup>1,2</sup> , Weiwei Chang <sup>3</sup>, Chao Yang <sup>1,2</sup>  and Jun Wang <sup>1,2,\*</sup>

<sup>1</sup> School of Materials Science and Engineering, Shanghai Jiao Tong University, Shanghai 200240, China; lijingjing-41422134@sjtu.edu.cn (J.L.); jujiang1990@sjtu.edu.cn (J.J.); yangchao1987@sjtu.edu.cn (C.Y.)

<sup>2</sup> Shanghai Key Laboratory of Advanced High-temperature Materials and Precision Forming, Shanghai Jiao Tong University, Shanghai 200240, China

<sup>3</sup> Institute for Advanced Materials and Technology, University of Science and Technology Beijing, Beijing 100083, China; s20181310@xs.ustb.edu.cn

\* Correspondence: junwang@sjtu.edu.cn

Received: 2 May 2020; Accepted: 25 May 2020; Published: 27 May 2020



**Abstract:** In this study, a high aluminum and chromium Fe-B-C coating was prepared using laser cladding on 2Cr13 steel substrate. The microstructure, microhardness, and wear resistance of the high aluminum and chromium Fe-B-C coating were investigated. The results show that this dense coating possesses good metallurgical bond with the substrate. The microstructure is mainly composed of  $\alpha$ -(Fe, Cr, Al) lath martensite, orthorhombic  $M_2B$  boride, orthogonal  $M_3C_2$ , and orthorhombic  $M_7C_3$  carbides. The microhardness of the coating can reach 620 HV which is 3.3-times higher than that (190 HV) of the substrate. The coating shows a lower friction coefficient of 0.75 than that of the substrate (1.08). The wear rates of the substrate and the coating are 0.295 mg/min and 0.103 mg/min, respectively, indicating the coating exhibits excellent wear resistance. The wear mechanism transforms severe adhesive wear and abrasive wear of the substrate to slight abrasive wear of the coating. The results can provide technical support to improve the properties of the Fe-based laser cladded coating.

**Keywords:** Fe-based coating; laser cladding; transmission electron microscopy (TEM); microstructure; wear resistance

## 1. Introduction

With the rapid development of the world economy, global energy demand is steadily on the increase [1,2]. The non-renewable fossil fuels accounts for more than 80% of the total energy, which puts forward higher request to the mining equipment [3,4]. The wear of the metal parts is one of the main problems affecting the service life of mining equipment. Thus, it is urgent and crucial to improve the wear resistance of mining equipment [5].

Laser cladding technology is a material surface modification method for improving the wear resistance of alloys [6]. It can fabricate a coating with special physical, chemical, or mechanical properties using a high energy laser beam [7]. Compared with traditional spraying processes, the laser cladding technology possesses four advantages: (1) Good metallurgical bonding with low dilution; (2) High yield and small margin for subsequent processing; (3) precise control, online control and remote manipulation for the repair of local and critical parts; and (4) low cost [8–10].

The coatings for laser cladding mainly consist of Fe-based, Co-based, Ni-based, ceramics, etc. [11]. Co-based and Ni-based coatings are characterized by high hardness, excellent wear resistance, heat resistance, and oxidation resistance. However, the cost of Co-based and Ni-based alloys is very high [12,13]. Ceramic coatings have much better properties in comparison with metal coatings, but its

brittleness has always been an obstacle to its wide application [14]. Hence, Fe-based coatings attract more and more attention due to their low cost and high performance [15]. Many scholars have studied the improvement of wear resistance of materials by Fe-based coatings via laser cladding [16]. W.J. Wang et al. fabricated Fe-Cr-Ni-B composite coating with high hardness and good wear resistance on wheel and rail materials using laser cladding [17]. Zhang et al. studied the microstructure, wear resistance and corrosion resistance of Fe-Ti-V-Cr-C-CeO<sub>2</sub> coating, and found the coating possessed good wear and corrosion resistance [18].

H.G. Fu et al. found the addition of Al and Cr can significantly enhance the microhardness, wear resistance and oxidation resistance Fe-B coatings [19–21]. In this study, the high aluminum and chromium Fe-B-C coating was fabricated using laser cladding technology on the 2Cr23 steel substrate. The microstructure, microhardness and wear resistance of the high aluminum and chromium Fe-B-C coating was investigated.

## 2. Materials Fabrication and Experimental Methods

### 2.1. Materials Fabrication

The 2Cr13 steel (corresponding to 420 steel, US ASTM Standards) with a dimension of 150 mm × 150 mm × 10 mm was used to the substrate, its chemical compositions are 0.22 wt.% C, 12.9 wt.% Cr, 0.4 wt.% Si, 0.61 wt.% Mn, 0.016 wt.% S, 0.018 P wt.%, and the balance Fe. The microstructure of the 2Cr13 substrate is mainly composed of the  $\alpha$ -Fe matrix and the M<sub>23</sub>C<sub>6</sub> carbides distributed along the grain boundaries, as shown in Figure 1. The 2Cr13 substrate was grinded using the 1000# SiC sandpaper, and then cleaned by alcohol and acetone. High aluminum and chromium Fe-B-C powder was proportioned with pure alloy powder with a size of 60–80  $\mu$ m. The prepared high aluminum and chromium Fe-B-C powder was dried in a drying oven to remove moisture, and then put into a ball mill pot in a glove box and ground at 120 r/min for 4 h. The chemical compositions of high aluminum and chromium Fe-B-C powder after mixing were measured by inductively coupled plasma mass spectrometry (ICP-MS), as shown in Table 1.

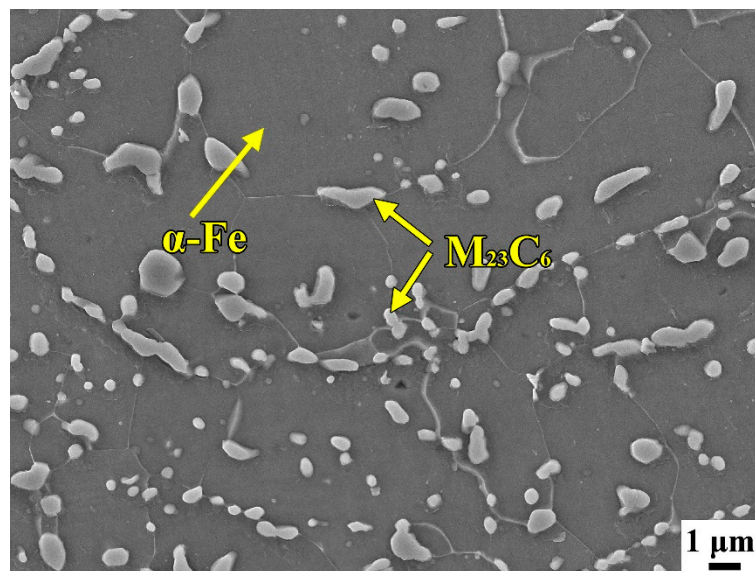


**Figure 1.** The microstructure image of the 2Cr13 steel substrate.

**Table 1.** The chemical compositions of the high aluminum and chromium Fe-B-C cladding powder (wt.%).

Elements	Al	Cr	B	Si	Mn	C	Fe
Content	6.0	10.0	1.5	0.6	0.7	0.3	Bal.

In this study, IPG-6000 optical fiber laser cladding system was used for laser cladding. First, a layer of high aluminum and chromium Fe-B-C powder with a thickness of 1 mm was prefabricated on 2Cr13 steel plate. The binder was cellulose acetate ( $C_6H_8O_3(COOCH_3)_2$ )<sub>n</sub>. Before laser cladding, the 2Cr13 substrate was preheated to 80 °C to reduce cracking. The main parameters are 2.5 kW laser power, 4 mm/s scanning speed, 15 L/min-Ar gas flow speed, and 5 mm × 5 mm spot size. The metallographic sample with a size of 10 mm × 10 mm × 5 mm was prepared by wire cutting. After grinding and polishing, it was cleaned using acetone and alcohol for 60 s.

## 2.2. Phase Diagram Calculation

Thermo-Calc<sup>®</sup> software was used to calculate the phase diagram. The mass percent of each element was C-0.3 wt.%, Cr-10.0 wt.%, Al-6.0 wt.%, Si-0.6 wt.%, Mn-0.7 wt.%, and the balance Fe. The content of B varied from 0.0 to 3.0 wt.%. The POLY-3 module provided initial conditions for the phase diagram calculations, such as composition, temperature, activity etc. The thermodynamic data for each substance was provided by the TCFE8 database. Furthermore, multivariate and multiphase equilibrium calculations were performed. The temperature range was 0–1750 °C, and the pressure was 105 kPa.

## 2.3. Microhardness and Wear Resistance Tests

The microhardness was measured using the MICRO MET-5103 Digital micrometer. The normal load was 4.9 N, the load time was 10 s. The UMT-3 reciprocating wear tester was conducted to test the wear resistance. The Al<sub>2</sub>O<sub>3</sub> ceramic ball with Ø 4 mm was the grinding material, its microhardness is 1300 HV [21]. The load was 20 N, the reciprocating stroke was set as 5 mm, the frequency was 1 Hz. The wear time and the sliding speed were 60 min and 0.1 m/s, respectively. The wear resistance was evaluated using wear rate ( $W_r$ ,  $g^3 \cdot N^{-1} \cdot min^{-1}$ ) which can be calculated according to the following Equation (1) [22]:

$$W_r = \frac{w_{loss}}{F_n \times t} \quad (1)$$

where  $w_{loss}$  represents the total wear loss (mg),  $F_n$  is the normal load (N) and  $t$  is the wear time (s). The microhardness and wear tests were repeated three times for each sample to ensure more accurate experimental data.

## 2.4. Characterization

The samples were ground on SiC papers with granulations of 240, 400, 600, 800, 1200, 1500, 2000, and 3000 and polished using diamond suspensions. The samples were etched using 5% FeCl<sub>3</sub> solution. The microstructure and compositional analyses of various phases were performed using a Mira 3 scanning electron microscope (SEM), transmission electron microscopy (TEM) and a JXA-8230 electron probe micro-analyzer (EPMA). The EPMA parameters were set to the 15 kV acceleration voltage, 10 nA beam current and 1 μm beam spot diameter. The standard sample was pure material (such as pure Al, Fe etc.). X-ray diffraction (XRD) was performed on a SHIMADZU Japan XRD-7000 diffractometer with copper K $\alpha$  radiation coupling continuous scanning at 40 kV and 200 mA as the X-ray source. The specimen was scanned in the angular 2 $\theta$  ranging from 20° to 80° with a step size of 0.2° and a collection time of 10 s.

# 3. Results and Discussions

## 3.1. Phase Diagram and Phase Structure

The vertical sections of high aluminum and chromium Fe-B-C coatings were calculated using Thermo-Calc<sup>®</sup> software, as shown in Figure 2. From Figure 2, under the condition of the equilibrium solidification, Cr<sub>2</sub>B phase precipitates directly from the liquid phase when the concentration of B is 1.5 wt.%. The eutectic reaction of L →  $\delta$ -Fe + Cr<sub>2</sub>B occurs at about 1400 °C, precipitating  $\delta$ -Fe phase.

As the temperature continues to reduce, the remaining liquid phase transform into the  $\gamma$ -Fe, forming the  $\delta$ -Fe +  $\gamma$ -Fe +  $\text{Cr}_2\text{B}$  three-phase zone. When the temperature drops to about 900 °C, the  $\text{M}_7\text{C}_3$  phase gradually precipitates. It can be seen that the equilibrium microstructure consists mainly of  $\alpha$ -Fe +  $\text{Cr}_2\text{B}$  +  $\text{M}_3\text{C}_2$  at room temperature. In addition, the  $\text{M}_7\text{C}_3$  and  $\text{Fe}_3\text{Al}$  phase may be obtained when the B content is less and greater than 1.5 wt.%, which also may be obtained under the rapid cooling.

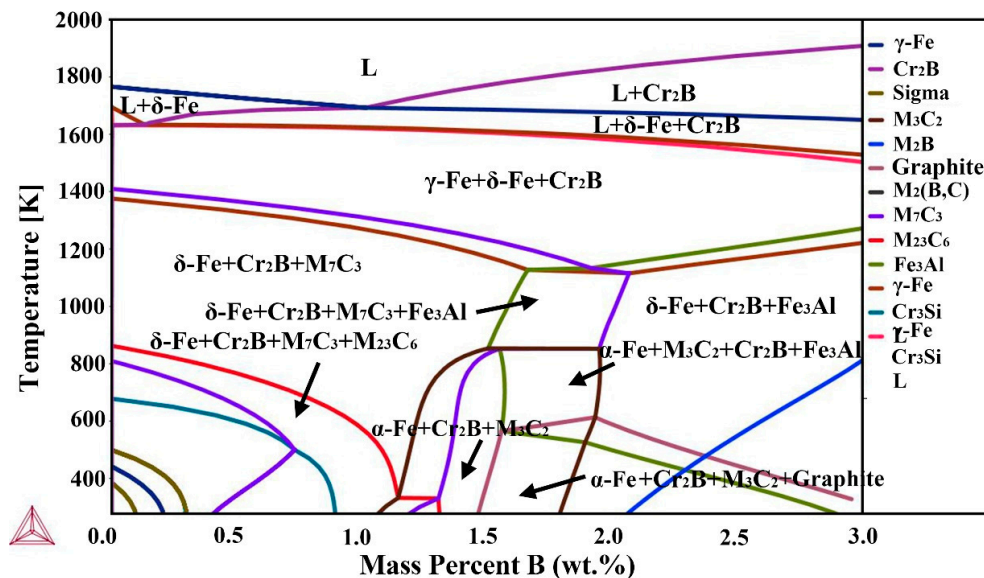


Figure 2. The calculated vertical sections of Fe-Cr-B-Al-C high aluminum and chromium Fe-B-C coatings.

### 3.2. Microstructure

Figure 3 shows the microstructure morphologies of high aluminum and chromium Fe-B-C coating. From Figure 3a, the coating is uniform and dense, and no defects such as pores and cracks are found. Figure 3b shows the coating has a good metallurgical bonding with the substrate. The interface bonding zone is a thick planar crystal, which gradually develops into columnar crystal and dendritic crystal of the cladding layer. The microstructure of coating mainly depends on the ratio value of temperature gradient  $G$  to the solidification rate  $R$  [23]. There is a large temperature gradient at the interface between the substrate and the molten pool, the solidification rate  $R$  tends to zero, this makes the  $G/R$  value tends to infinity. Therefore, the microstructure grows epitaxy as a planar crystalline from the substrate. As the solidification proceeds, the temperature gradient decreases due to the decreasing molten pool temperature, leading to the dropping of the  $G/R$  value. The microstructure changes from planar crystal to columnar crystal. The dendritic crystals are formed in the middle and upper part of the coating with a decrease of the  $G/R$  value, as shown in Figure 3c.

Figure 4 presents the X-ray pattern results of the coating. The matrix occupies the peak location ( $2\theta = 44.49^\circ$ ,  $64.31^\circ$ , and  $81.97^\circ$ ) of the  $\alpha$ -Fe, which is slightly less than the peak values ( $2\theta = 44.69^\circ$ ,  $64.96^\circ$ , and  $82.36^\circ$ ) of  $\alpha$ -Fe in 2Cr13 steel [24]. The compositions of various phases were detected by EPMA, as shown in Table 2. It can be seen that the elements Cr, Al, etc. are dissolved into the  $\alpha$ -Fe. Moreover, the atomic radii of Fe and Cr are 118 and 117 pm respectively, which is very helpful for Cr to be solidly dissolved in  $\alpha$ -Fe, resulting in lattice mismatches, leading to a left shift of  $2\theta$  [25]. The Al and Cr elements dissolve into the matrix to form  $\alpha$ -(Fe, Cr, Al) solid solution. The eutectic microstructure is mainly composed of  $\text{M}_2\text{B}$  borides and  $\text{M}_3\text{C}_2$  and  $\text{M}_7\text{C}_3$  carbides, M mainly represents the elements of Fe, Cr, etc. [26]. The contents of Cr, B, and C in the eutectic phase zone 2 and zone 3 are much higher than that in dendrite (zone 1), while the contents of Fe, Al, and Si are higher in dendrite. This indicates that Cr element is easy to form boroncarbides among dendrites, while Al element are easier to be solidly dissolved into matrix to form matrix  $\alpha$ -(Fe, Cr, Al) solid solution, which is conducive to improving the hardness and wear resistance of the coating.

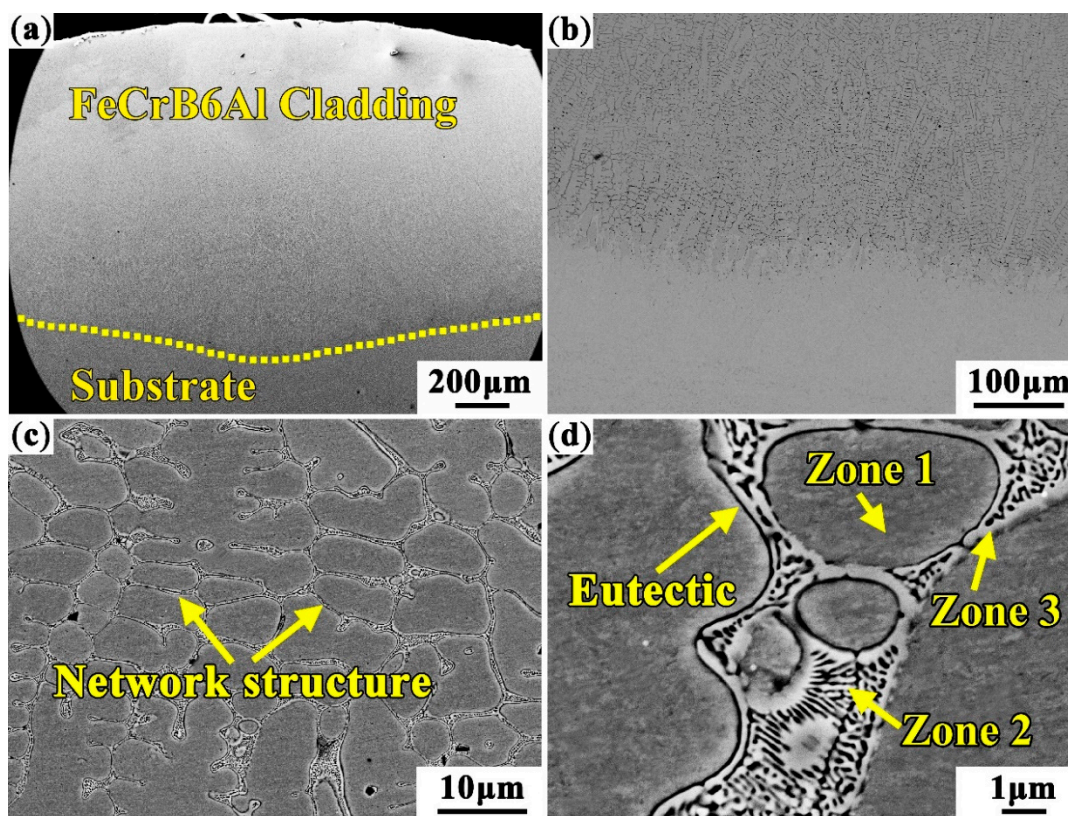


Figure 3. The microstructure morphologies of high aluminum and chromium Fe-B-C coating: (a) Macromorphology; (b) Bottom of cladding layer; (c,d) Middle part of cladding layer.

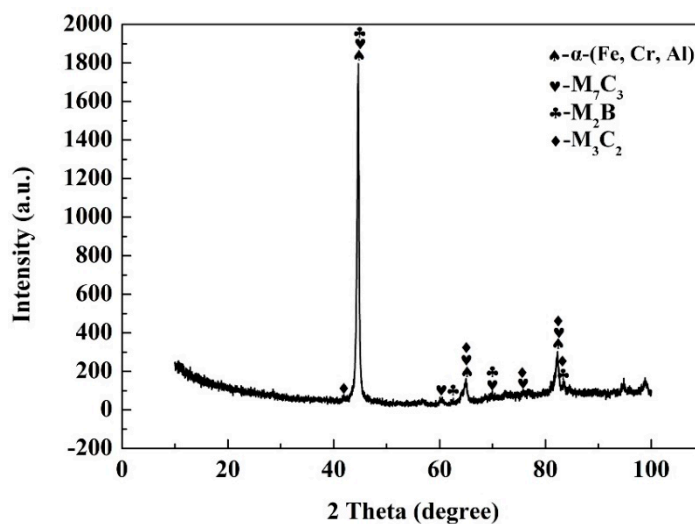
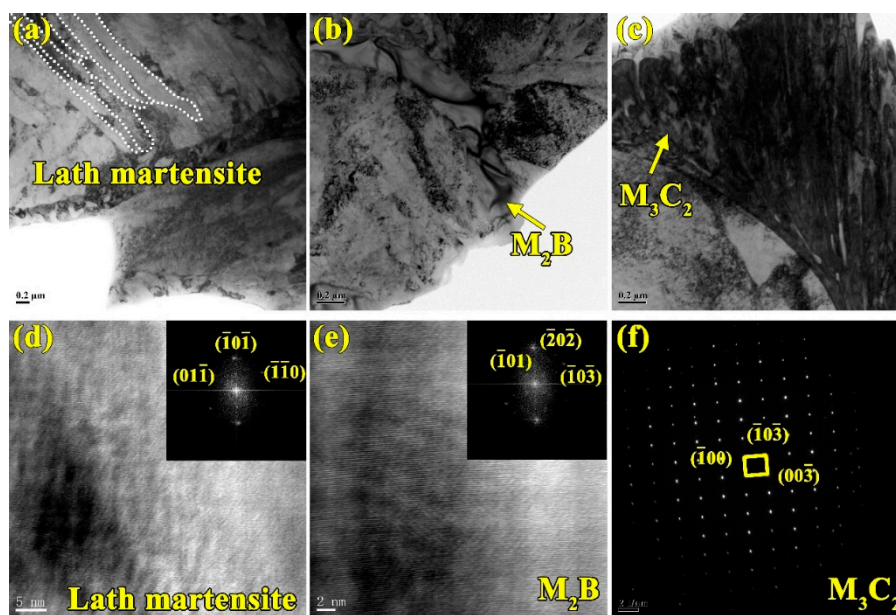


Figure 4. The X-ray pattern of high aluminum and chromium Fe-B-C coating.

Table 2. Chemical compositions of the phases with different morphologies in high aluminum and chromium Fe-B-C coating (wt.%).

Content	Fe	Cr	B	Al	Si	Mn	C
Zone1	84.175	12.271	0.44	2.271	0.494	0.628	0.554
Zone2	80.647	13.756	0.926	1.808	0.465	0.664	1.259
Zone3	70.813	21.483	3.623	0.692	0.193	0.837	3.105

The TEM tests are conducted to further determine the type of matrix and interdendritic boroncarbides in coating, as shown in Figure 5. From Figure 5a,d, the matrix of the coating is identified as the lath martensite with face-centered-cubic (fcc) structure. The large-sized block phase formed between dendrites are orthorhombic  $M_2B$ , and the small rod-shaped phase between the block  $M_2B$  are  $M_3C_2$  with orthogonal structure and  $M_7C_3$  with orthorhombic structure carbides. This network structure of eutectic structure is very similar to the microstructure of the cast Fe-Cr-B-Al alloy [27]. The size and distribution of the  $M_2B$  borides,  $M_3C_2$  and  $M_7C_3$  carbides in coating mostly depend on the microstructure evolution mechanism from the initial reactant powders. It is very interesting to study the microstructure evolution mechanism during the laser cladding. The powders dissolve into atoms in the molten pool under the laser beam, the  $Cr_2B$  phase firstly precipitates from the molten pool during the solidification according to the results in Figure 2. From Figure 3d, it can be speculated that as solidification process progresses, the remaining atoms begin to nucleate and grow on the  $Cr_2B$  and the  $M_7C_3$  and  $M_3C_2$  precipitates.



**Figure 5.** Transmission Electron Microscopy (TEM) of high aluminum and chromium Fe-B-C coating: (a–c) bright field images; (d) high resolution image of lath martensite and corresponding selective area diffraction (SAD) pattern; (e) high resolution image of  $M_2B$  and corresponding SAD pattern; and (f) the SAD pattern of  $M_3C_2$ .

### 3.3. Microhardness

Figure 6 shows the microhardness profile along the cross-section of the coating. It can be seen that the microhardness exhibits a gradient variation from the substrate to the coating, gradually increases from the interface bonding zone, heat-affected zone to the coating, which is mainly connected with microstructure evolution of the coating. According to the results of microstructure analysis, the microstructure gradually transforms columnar crystals to equiaxed grains from the substrate to the coating. H. Xie et al. reported the hardness of the equiaxed grains is much higher than that of the columnar grains [28]. J. Li et al. thought the heat-affected zone (HAZ), as a transition zone, can effectively decrease the stress concentration and enhance the interface bonding [29]. It also can be seen that the microhardness of the coating has no major fluctuation and reaches 620 HV, which is 3.3 times that (190 HV) of the substrate. This indicates the microstructure is very evenly distributed and no obvious cracks and holes defects were produced. According to the microstructure analysis, the matrix of the coating is the  $\alpha$ -(Fe, Cr, Al) solid solution martensite. The Al and Cr elements plays a solid solution strengthening role. The microhardness of martensite (480–560 HV) is higher than that

of the ferrite (160–220 HV) [30]. Furthermore, the  $M_2B$  borides,  $M_3C_2$  and  $M_7C_3$  carbides with high hardness precipitates in the coating. Z.F. Huang found the microhardness of  $Fe_2B$  is about 1500 HV [31], furthermore, J. Lentz found the hardness of the  $M_2B$  is lightly higher than that of the  $Fe_2B$  [32,33]. The hardness of  $M_7C_3$  is reported to be about 1800 HV by Tassin [34]. H.G. Fu et al. found the hardness of the  $M_3C_2$  is slightly lower than that of the  $Fe_2B$  about 1300 HV [35]. The martensitically hardened Fe matrix and the high hardness of the hard phases lead to an improvement of microhardness of the coating.

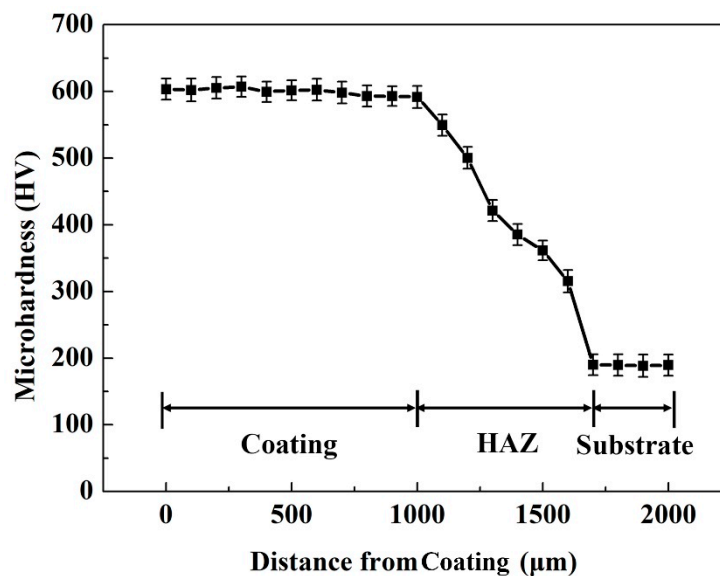
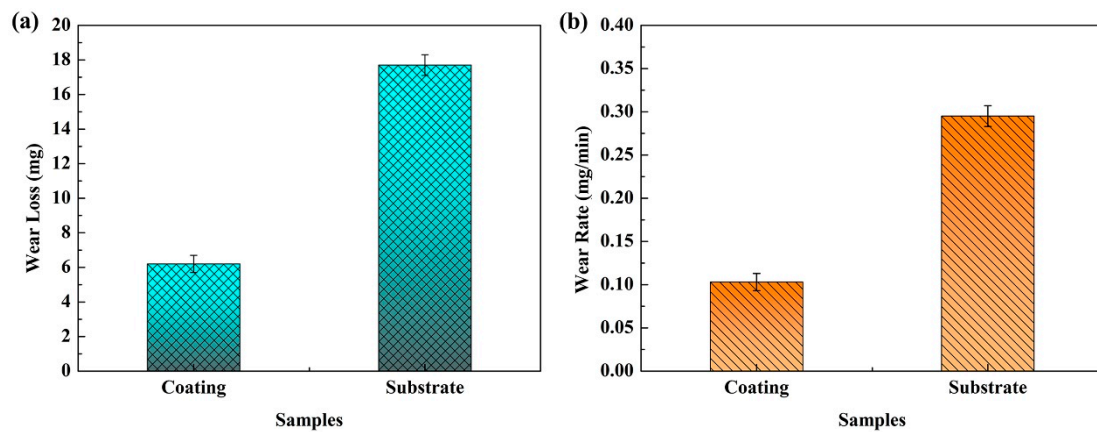


Figure 6. The microhardness profile along the cross-section of the coating.

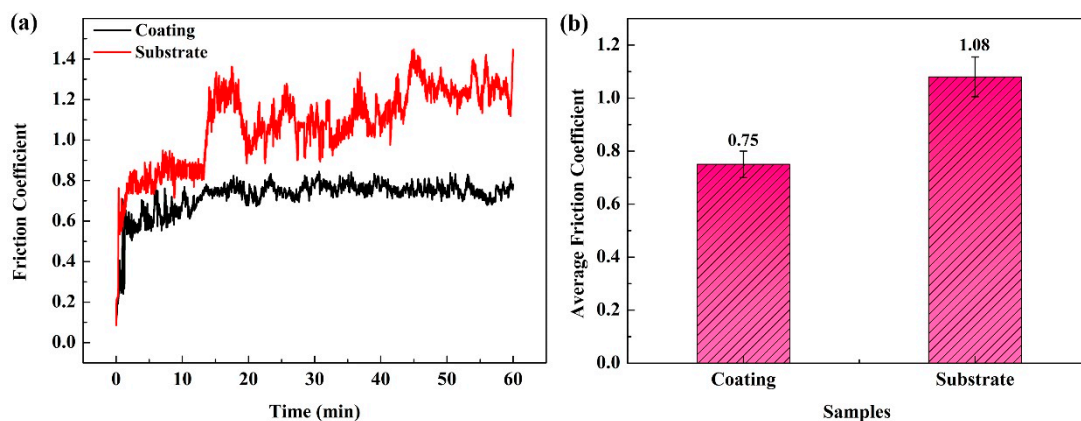
### 3.4. Wear Resistance

Figure 7 shows the wear loss and wear rate of the substrate and coating. As can be seen from Figure 7a, the wear loss of substrate reaches 17.7 mg, while that of the coating is only 6.2 mg. According to Equation (1), the calculated wear rates of the coating and substrate are 0.295 mg/min and 0.103 mg/min, respectively, as shown in Figure 7b. The wear resistance of laser cladded coating is ~2-times higher than that of substrate. H. Berns studied the effect of B/C on wear resistance of the as-cast Fe-B-C alloy, and found the as-cast Fe-B-C alloy exhibited excellent wear resistance due to the main  $Fe_3(C,B)$  phase with high hardness ( $1300 \pm 50$  HV) when the B/C was 1/3 [36]. According to the microstructure analysis, the Al and Cr elements dissolve into the matrix to form  $\alpha$ -(Fe, Cr, Al) solid solution, furthermore, the  $M_2B$  borides and  $M_7C_3$  and  $M_3C_2$  carbides of the coating have high hardness, which is higher than the  $Fe_3(B,C)$  phase, exhibiting better wear resistance. The high hardness borides and carbides can inhibit the wear of the grinding ball on the matrix, while the matrix with high hardness can also prevent the boron-carbons from falling off. The boroncarbide network structure in the coating makes it more stable, while the  $M_{23}C_6$  carbides in the substrate are mainly distributed along grain boundaries, and the microhardness of  $\alpha$ -Fe matrix is lower than that of the martensite. After the application of the load, the  $M_{23}C_6$  carbides with high hardness may be pressed into the matrix, resulting in severe cutting to the matrix. The reciprocating wear can further aggravate the wear of the substrate.



**Figure 7.** The wear loss (a) and wear rate (b) of the tested samples.

Figure 8 presents the variation of friction coefficient with time and average friction coefficient of the tested samples. It can be seen that the friction coefficient of the substrate increases quickly and remain stable in the first 12 min, and exhibits large fluctuation in the subsequent wear process which is caused by the incomplete occlusal of samples and grinding balls. Comparing with the friction coefficient of the substrate, the fluctuation of friction coefficient of the coating decreases significantly, as shown in Figure 8a. From Figure 8b, it is clear that the average friction coefficient of the coating is 0.75, which is much lower than that of the substrate (1.08).



**Figure 8.** The variation of friction coefficient with time (a) and average friction coefficient (b) of the tested samples.

### 3.5. Wear Mechanisms

Figure 9 shows the morphologies of the worn surface of the tested samples. It can be seen that large pits and abrasive particles can be observed on the worn surface of the substrate, as shown in Figure 9a, which indicates the wear mechanism of the substrate is composed of the adhesive wear and abrasive wear. However, the worn surface of the coating shows a completely different morphology. A lot of shallow furrows appear on the worn surface, and contains some abrasive particles with small size. The formation of the abrasive particles causes the three body abrasion, which may be the main reason for forming the furrows. This suggests the wear mechanism of the coating is mainly comprised of slight abrasive wear.

The wear resistance of materials is mainly related to morphology and microstructure [37]. The substrate is composed of soft  $\alpha$ -Fe matrix and little hard  $M_{23}C_6$  carbides distributed along the grain boundary [38]. The soft matrix does not provide adequate protection for hard  $M_{23}C_6$  carbides, resulting in the peeling off of hard carbides. This also is the main reason to bring about the fluctuation

of friction coefficient of substrate. The martensite and network structure comprising of  $M_2B$  borides and  $M_7C_3$  and  $M_3C_2$  carbides are observed in the coating, as shown in Figure 5c,d. The martensite is stiffer than  $\alpha$ -Fe ferrite, which suppresses the falling off of the hard phase. Moreover, the hard phases such as  $M_2B$  borides and  $M_7C_3$  and  $M_3C_2$  carbides exhibit network structure. Compared with granular and block  $M_{23}C_6$  carbides in the substrate, these continuous network structures are more resistant to abrasion, which can protect the martensitic matrix, thus the wear resistance of the coating is improved.

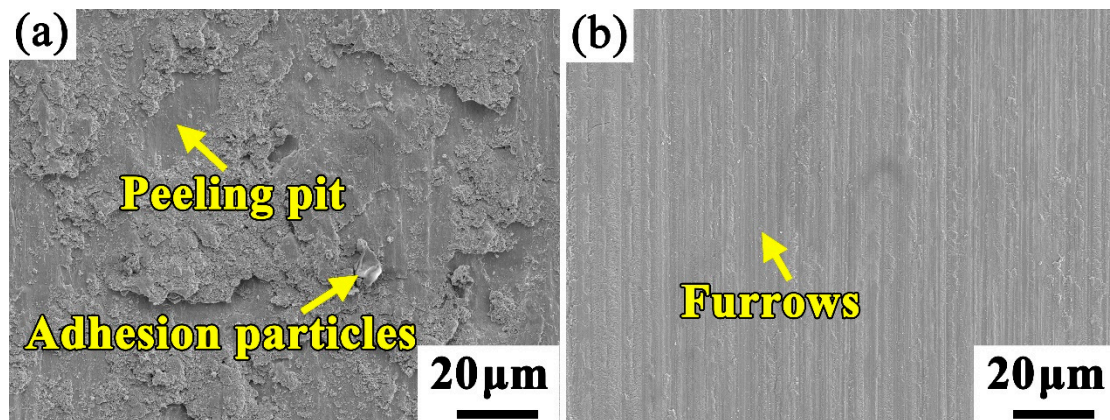


**Figure 9.** The morphologies of the worn surface of (a) substrate and (b) high aluminum and chromium Fe-B-C coating.

#### 4. Conclusions

A novel high aluminum and chromium Fe-B-C coating which compositions are designed using the Thermo-Calc<sup>®</sup> software was fabricated using laser cladding technology. The microstructure, microhardness and wear resistance were systematically investigated. The main conclusions of this research can be drawn as follows:

1. The coating is dense and has good metallurgical bond with the substrate. The microstructure is mainly composed of  $\alpha$ -(Fe, Cr, Al) lath martensite, orthorhombic  $M_2B$  borides, orthogonal  $M_3C_2$ , and orthorhombic  $M_7C_3$  carbides.
2. The microhardness of the coating can reach to 620 HV which is 3.3-times higher than that of the substrate (190 HV). This is mainly due to the formation  $\alpha$ -(Fe, Cr, Al) lath martensite,  $M_2B$  borides, and  $M_3C_2$  and  $M_7C_3$  carbides with high hardness.
3. The coating shows lower friction coefficient of 0.75 than that of the substrate (1.08). The wear rate of the substrate and the coating are 0.295 and 0.103 mg/min, respectively, indicating the coating exhibits excellent wear resistance. The wear mechanism transforms severe adhesive wear and abrasive wear of the substrate to slight abrasive wear of the coating.

**Author Contributions:** Investigation, formal analysis, writing—original draft preparation, J.L.; software, writing—review and editing, J.J.; writing—review and editing, W.C. and C.Y.; supervision, writing—review and editing, project administration, funding acquisition, J.W. All authors have read and agreed to the published version of the manuscript.

**Funding:** The authors appreciate the financial support for this work from The National Key Research and Development Program of China (2016YFB0701405), Aeronautical Science Foundation of China (2016ZE57010), New Young Teachers Initiation Program Fund (18X100040027) and the China Postdoctoral Science Foundation (19Z102060057).

**Conflicts of Interest:** The authors declare that they have no known competing financial interests or personal relationships that could have appeared to influence the work reported in this paper.

## References

1. Kenneth, H.; Paivi, K.R.; Pirita, H.; Kati, V.; Ali, E. Global energy consumption due to friction and wear in the mining industry. *Tribol. Int.* **2017**, *115*, 116–139.
2. Ge, S.R.; Wang, Q.L.; Wang, J.X. The impact wear-resistance enhancement mechanism of medium manganese steel and its applications in mining machines. *Wear* **2017**, *376–377*, 1097–1104. [[CrossRef](#)]
3. Fleury, R.M.N.; Salvati, E.; Nowell, D.; Korsunsky, A.M.; Silva, F.; Tai, Y.H. The effect of surface damage and residual stresses on the fatigue life of nickel superalloys at high temperature. *Int. J. Fatigue* **2019**, *119*, 34–42. [[CrossRef](#)]
4. Li, M.Y.; Han, B.; Song, L.M.; He, Q.K. Enhanced surface layers by laser cladding and ion sulfurization processing towards improved wear-resistance and self-lubrication performances. *Appl. Surf. Sci.* **2020**, *503*, 144226. [[CrossRef](#)]
5. Makwana, D.; Bhingole, P.P. Electrochemical and plasma surface modification of magnesium and its alloy. *Mater. Today Proc.* **2019**, *5*, 18260–18267. [[CrossRef](#)]
6. Li, D.; Gou, G.Q.; Liu, Y.; Zhu, T.H.; Ji, H.; Chen, H. Effect of Al on microstructure and impact property of surfacing repair layer of rail. *Surf. Eng.* **2012**, *28*, 548–553. [[CrossRef](#)]
7. Zhan, X.; Qi, C.; Zhou, J.; Liu, L.; Gu, D. Effect of heat input on the subgrains of laser melting deposited Invar alloy. *Opt. Laser Technol.* **2019**, *109*, 577–583. [[CrossRef](#)]
8. Luo, X.; Li, J.; Li, G.J. Effect of NiCrBSi content on microstructural evolution, cracking susceptibility and wear behaviors of laser cladding WC/Ni–NiCrBSi composite coatings. *J. Alloys Compd.* **2015**, *626*, 102–111. [[CrossRef](#)]
9. Lv, Y.H.; Li, J.; Tao, Y.F.; Hu, L.F. High-temperature wear and oxidation behaviors of TiNi/Ti<sub>2</sub>Ni matrix composite coatings with TaC addition prepared on Ti<sub>6</sub>Al<sub>4</sub>V by laser cladding. *Appl. Surf. Sci.* **2017**, *402*, 478–494. [[CrossRef](#)]
10. He, X.; Song, R.G.; Kong, D.J. Microstructures and properties of Ni/TiC/La<sub>2</sub>O<sub>3</sub> reinforced Al based composite coatings by laser cladding. *Opt. Laser Technol.* **2019**, *117*, 18–27. [[CrossRef](#)]
11. Wang, K.M.; Du, D.; Liu, G.; Chang, B.H.; Ju, J.; Sun, S.T.; Fu, H.G. Microstructure and property of laser clad Fe-based composite layer containing Nb and B<sub>4</sub>C powders. *J. Alloys Compd.* **2019**, *802*, 373–384. [[CrossRef](#)]
12. Ma, Q.; Li, Y.; Wang, J.; Liu, K. Investigation on cored-eutectic structure in Ni60/ WC composite coatings fabricated by wide-band laser cladding. *J. Alloys Compd.* **2015**, *645*, 151–157. [[CrossRef](#)]
13. Sun, S.; Fu, H.; Chen, S.; Ping, X.; Wang, K.; Guo, X.; Lin, J.; Lei, Y. A numerical experimental investigation of heat distribution, stress field and crack susceptibility in Ni60A coatings. *Opt. Laser Technol.* **2019**, *117*, 175–185. [[CrossRef](#)]
14. Zhang, J.B.; Zhang, J.J.; Xiao, G.C.; Chen, Z.Q.; Yi, M.D.; Zhang, Y.B.; Xu, C.H. Orientational effect of graphene on the friction and wear behavior of Si<sub>3</sub>N<sub>4</sub>/TiC based composite ceramic tool materials. *Ceram. Int.* **2020**, *46*, 3550–3557. [[CrossRef](#)]
15. Zhao, Y.; Yu, T.B.; Guan, C.; Sun, J.Y.; Tan, X.F. Microstructure and friction coefficient of ceramic (TiC, TiN and B<sub>4</sub>C) reinforced Ni-based coating by laser cladding. *Ceram. Int.* **2019**, *45*, 20824–20836. [[CrossRef](#)]
16. Wang, C.; Zhang, S.; Zhang, C.H.; Wu, C.L.; Zhang, J.B.; Abdullah, A.O. Phase evolution and wear resistance of in situ synthesized V<sub>8</sub>C<sub>7</sub> particles reinforced Fe-based coating by laser cladding. *Opt. Laser Technol.* **2018**, *105*, 58–65. [[CrossRef](#)]
17. Fu, Z.K.; Ding, H.H.; Wang, W.J.; Liu, Q.Y.; Guo, J.; Zhu, M.M. Investigation on microstructure and wear characteristic of laser cladding Fe-based alloy on wheel/rail materials. *Wear* **2015**, *330–331*, 592–599. [[CrossRef](#)]
18. Zhang, H.; Zou, Y.; Zou, Z.D.; Wu, D.T. Microstructure and properties of Fe-based composite coating by laser cladding Fe-Ti-V-Cr-C-CeO<sub>2</sub> powder. *Opt. Laser Technol.* **2015**, *65*, 119–125. [[CrossRef](#)]
19. Ju, J.; Fu, H.G.; Lei, Y.P. Effect of Al addition on microstructure and properties of an Fe-B-Al alloy. *Mater. Test.* **2016**, *58*, 753–762. [[CrossRef](#)]
20. Ju, J.; Kang, M.D.; Wang, K.M.; Zhou, Y.; Jiang, M.; Zhao, Y.Y.; Zhang, Z.; Wang, J.; Fu, H.G. Studies on as-cast microstructure and oxidation behavior of the Fe-Cr-B-Al alloys at 1073 K. *Vacuum* **2019**, *164*, 436–448. [[CrossRef](#)]

21. Ju, J.; Yang, C.; Ma, S.Q.; Kang, M.D.; Wang, K.M.; Li, J.J.; Fu, H.G.; Wang, J. Effect of temperature on oxidation resistance and isothermal oxidation mechanism of novel wear-resistant Fe-Cr-B-Al-C-Mn-Si alloy. *Corros. Sci.* **2020**, *170*, 108620. [[CrossRef](#)]
22. An, Q.; Huang, L.J.; J, S.; Wang, S.; Zhang, R.; Sun, F.B.; Moridi, A.; Geng, L. Wear rate of titanium matrix composite coating at high temperature further increased by non-stoichiometric  $Ti_xC$  oxidation. *Ceram. Int.* **2020**, *46*, 8068–8074. [[CrossRef](#)]
23. Ju, J.; Zhou, Y.; Kang, M.D.; Wang, J. Optimization of process parameters, microstructure and properties of laser cladding Fe-Based Alloy on 42CrMo steel roller. *Materials* **2018**, *11*, 2061. [[CrossRef](#)] [[PubMed](#)]
24. Monson, P.J.E.; Steen, W.M. Comparison of Laser Hardfacing with Conventional Processes. *Surf. Eng.* **1990**, *6*, 185–193. [[CrossRef](#)]
25. Lyu, Y.Z.; Sun, Y.F.; Jing, F.Y. On the microstructure and wear resistance of Fe-based composite coatings processed by plasma cladding with  $B_4C$  injection. *Ceram. Int.* **2015**, *41*, 10934–10939. [[CrossRef](#)]
26. Wang, M.M.; Gao, R.; Gao, H.Y.; Zhou, Y.; Fan, Y.Y.; Zhao, Y.Y.; Ju, J.; Liu, Y.H.; Kang, M.D.; Wang, J. Improved corrosion resistance of Ni-modified Fe-Cr-B steel in molten zinc via phase transformation and microstructure control. *Surf. Coat. Technol.* **2013**, *235*, 811–818. [[CrossRef](#)]
27. Lv, Z.; Fu, H.G.; Xing, J.D.; Ma, S.Q.; Hu, Y. Microstructure and crystallography of borides and mechanical properties of Fe-B-C-Cr-Al alloys. *J. Alloys Compd.* **2016**, *662*, 54–62. [[CrossRef](#)]
28. Luo, X.X.; Cao, J.; Meng, G.H.; Chuan, Y.Y.; Yao, Z.J.; Xie, H. Systematical investigation on the microstructures and tribological properties of Fe-Al laser cladding coatings. *Appl. Surf. Sci.* **2020**, *516*, 146121. [[CrossRef](#)]
29. Jiang, J.S.C.; Li, J.B.; Lee, S.L.; Chang, Y.S.; Jian, S.R.; Huang, J.C.; Nieh, T.G. Prominent plasticity of Mg-based bulk metallic glass composites by ex-situ spherical Ti particles. *Intermetallics* **2012**, *30*, 25–29. [[CrossRef](#)]
30. Das Bakshi, S.; Shipway, P.H.; Bhadeshia, H.K.D.H. Three-body abrasive wear of fine pearlite, nanostructured bainite and martensite. *Wear* **2013**, *308*, 46–53. [[CrossRef](#)]
31. Huang, Z.F.; Xing, J.D.; Lv, L.L. Effect of tungsten addition on the toughness and hardness of  $Fe_2B$  in wear-resistant Fe-B-C cast alloy. *Mater. Charact.* **2013**, *75*, 63–68. [[CrossRef](#)]
32. Jonathan, L.; Arne, R.; Felix, G.; Werner, T. Enhancement of hardness, modulus and fracture toughness of the tetragonal  $(Fe,Cr)_2B$  and orthorhombic  $(Cr,Fe)_2B$  phases with addition of Cr. *Mater. Des.* **2018**, *156*, 113–124.
33. Jonathan, L.; Arne, R.; Werner, T. Hardness and modulus of  $Fe_2B$ ,  $Fe_3(C,B)$  and  $Fe_{23}(C,B)_6$  borides and carboborides in the Fe-C-B system. *Mater. Charact.* **2018**, *135*, 192–202.
34. Tassin, C.; Lroudie, F.; Pons, M.; Lelait, L. Carbide-reinforced coatings on AISI 326L stainless steel by laser surface alloying. *Surf. Coat. Technol.* **1995**, *76–77*, 450–455. [[CrossRef](#)]
35. Yang, Y.W.; Fu, H.G.; Lei, Y.P.; Wang, K.M.; Zhu, L.L.; Jiang, L. Phase diagram calculation and analyze on cast high-boron high-speed steel. *J. Mater. Eng. Perform.* **2016**, *25*, 409–420. [[CrossRef](#)]
36. Berns, H.; Anastasia, S.; Arne, R.; Dietrich, H. Wear Protection by Fe-B-C Hard Phases. *Steel Res. Int.* **2011**, *82*, 786–794. [[CrossRef](#)]
37. Janicki, D. Microstructure and sliding wear behavior of in-situ TiC-reinforced composite surface layers fabricated on ductile cast iron by laser alloying. *Materials* **2018**, *11*, 75. [[CrossRef](#)]
38. Liu, X.; Yang, J.C.; Yang, L.; Gao, X.Z. Effect of Ce on inclusions and impact property of 2Cr13 stainless steel. *J. Iron Steel Res. Int.* **2010**, *17*, 59–64. [[CrossRef](#)]

